



UNIVERSITY OF LEEDS

This is a repository copy of *Online Detection of Particle Agglomeration during Solution Crystallization by Microscopic Double-View Image Analysis*.

White Rose Research Online URL for this paper:
<http://eprints.whiterose.ac.uk/122286/>

Version: Accepted Version

Article:

Huo, Y, Liu, T, Wang, XZ et al. (2 more authors) (2017) Online Detection of Particle Agglomeration during Solution Crystallization by Microscopic Double-View Image Analysis. *Industrial & Engineering Chemistry Research*, 56 (39). pp. 11257-11269. ISSN 0888-5885

<https://doi.org/10.1021/acs.iecr.7b02439>

© 2017 American Chemical Society. This document is the Accepted Manuscript version of a Published Work that appeared in final form in *Industrial and Engineering Chemistry Research*, copyright © American Chemical Society after peer review and technical editing by the publisher. To access the final edited and published work see <https://doi.org/10.1021/acs.iecr.7b02439>

Reuse

Items deposited in White Rose Research Online are protected by copyright, with all rights reserved unless indicated otherwise. They may be downloaded and/or printed for private study, or other acts as permitted by national copyright laws. The publisher or other rights holders may allow further reproduction and re-use of the full text version. This is indicated by the licence information on the White Rose Research Online record for the item.

Takedown

If you consider content in White Rose Research Online to be in breach of UK law, please notify us by emailing eprints@whiterose.ac.uk including the URL of the record and the reason for the withdrawal request.



eprints@whiterose.ac.uk
<https://eprints.whiterose.ac.uk/>

On-line detection of particle agglomeration during solution crystallization by microscopic double-view image analysis

Yan Huo ^a, Tao Liu ^{a,*}, Xue Z. Wang ^{b,c}, Cai Y. Ma ^b, Xiongwei Ni ^d

^a Institute of Advanced Control Technology, Dalian University of Technology, Dalian, China

^b School of Chemical and Process Engineering, University of Leeds, Leeds, LS2 9JT, UK

^c School of Chemistry and Chemical Engineering, South China University of Technology, Guangzhou, China

^d School of Engineering and Physical Science, Heriot-Watt University, Edinburgh, UK

* Corresponding author. Tel: +86-411-84706465; Fax: +86-411-84706706; E-mail: liurouter@ieee.org

Abstract: To detect the particle agglomeration degree for assessing crystal growth quality during a crystallization process, an in-situ image analysis method is proposed based on a microscopic double-view imaging system. Firstly, a fast image preprocessing approach is adopted for segmenting raw images taken simultaneously from two cameras installed at different angles, to reduce the influence from uneven illumination background and solution turbulence. By defining an index of the inner distance based curvature for different particle shapes, a preliminary sieving algorithm is then used to identify candidate agglomerates. By introducing two texture descriptors for pattern recognition, a feature matching algorithm is subsequently developed to recognize pseudo agglomerates in each pair of the double-view images. Finally, a fast algorithm is proposed to count the number of recognized particles in these agglomerates, besides the unagglomerated particles. Experimental results from the potassium dihydrogen phosphate (KDP) crystallization process demonstrate good accuracy for recognizing pseudo agglomeration and counting the primary particles in these agglomerates by using the proposed method.

Keywords: particle agglomeration; pseudo agglomerate; double-view image analysis; feature matching; texture descriptor; particle counting

1. Introduction

On-line imaging systems have been increasingly applied to monitor industrial crystallization processes at the micro-scale in the last two decades ¹⁻⁵, offering on-line observation of the crystal shapes related to crystal morphology and growth rate. By using high-speed microscopic camera sensors, e.g., the particle vision and measurement (PVM) instrument ^{6,7} and the non-invasive imaging system⁸, a small number of image analysis methods were explored in the recent references ⁹⁻¹³ for on-line measurement of crystal size distribution (CSD) during a crystallization process. However, the influence from uneven illumination background and solution turbulence on in-situ imaging in a continuously stirred crystallizer was not fully considered in literature. Such influence may provoke significant misestimate of crystal morphology or CSD by using the existing image processing methods, as studied in the recent paper ¹⁴. Development of advanced in-situ image analysis methods has been eagerly appealed for on-line monitoring, control and optimization of various crystallization processes ^{3,15}.

Particle agglomeration is commonly associated with crystallization processes due to particle collisions in the stirred crystal suspension, which has a considerable impact on the crystal properties such as the dissolution rate, precipitation, filtration, drying, milling and grinding. It is one of the main tasks to control the agglomeration degree for industrial crystallization processes ¹⁶. Image-based detection of particle agglomeration has therefore been increasingly studied for on-line control and optimization. In the early study ¹⁷, detecting agglomerates from crystal images was performed off-line by using a statistical principal component analysis (PCA) approach. Ferreira et al. ¹⁸ presented an automatic classification tree to distinguish different classes of sucrose crystals and the agglomeration degree. Terdenge et al. ¹⁹ developed an image processing method based on a discriminant factorial analysis to evaluate the agglomeration degree of crystalline products. Ochsenbein et al. ²⁰ presented a machine learning method to identify the agglomeration of needle-like crystals together with the primary particles involved in these agglomerates. Borchert et al. ²¹ developed an image-based identification method for monitoring the growth rate of crystals such as the potassium dihydrogen phosphate (KDP) that is a typical case of morphology evolution for multi-dimensional CSD measurement and verification.

As a matter of fact, there occur a lot of pseudo agglomerates in single-view images taken from a

crystallization process, due to overlapped particles which have different distances to the camera lens. These pseudo agglomerates inevitably affect image-based measurement accuracy of CSD and the true agglomeration degree. To solve the problem, it was suggested to adopt double-view images for recognizing pseudo agglomerates²⁰, but how to realize exact feature matching for overlapped particles in each pair of double-view images remains open. Regarding feature matching between the double-view images taken for the same object, a widely recognized matching algorithm is the scale invariant feature transform (SIFT)²², where a 128-dimensional descriptor was established from a three-dimensional (3D) histogram of gradient locations and orientations, while using a weighting function of the gradient magnitude for each location bin to ensure efficient matching. An alternative interest point descriptor was proposed to construct another matching algorithm named ASIFT²³ which may procure improved matching effect in some cases, but at the cost of larger computation effort. To alleviate the computation load of SIFT, Bay et al.²⁴ developed a fast algorithm so called speeded up robust features (SURF), which computed the Haar wavelet responses via the integral images instead of the gradient information. By comparison, Rublee et al.²⁵ proposed a faster matching algorithm called ORB by using the binary descriptors, which demonstrated good robustness to rotational variation and measurement noise.

Note that particles in microscopic double-view images taken from a crystallization process typically have high similarity in the feature properties, thus bringing difficulty to feature distinction by using the aforementioned matching methods. To efficiently address the problem of feature similarity among these images, texture statistical analysis was adopted as an alternative descriptor for image matching in literature. By defining the local binary pattern (LBP)²⁶, both the statistical and structural characteristics of image texture were used for double-view image matching. A few modified LBP descriptors have been developed in the reference²⁷ for better texture classification and image recognition. To enhance the performance of LBP, a completed LBP modeling was developed for texture classification²⁸, which extracted the local gray levels and magnitude features among these images, respectively. The approach was further extended by defining the LBP variance (LBPV) to characterize the local contrast information in a one-dimensional LBP histogram for matching²⁹. By comparison, Liu et al.³⁰ proposed an LBP based neighboring intensities descriptor using only local neighborhood

distributions to represent consistent patterns. However, it remains open for implementing the above methods for on-line recognition of particle agglomeration in engineering applications, in particular for poor imaging conditions during a crystallization process.

In this paper, an in-situ double-view image analysis method is proposed for recognizing pseudo particle agglomeration during a crystallization process, by establishing a double-view image matching algorithm based on feature analysis. Firstly, an image preprocessing strategy is used to reduce the influence from uneven illumination background, solution turbulence, and measurement noise. Then a preliminary sieving algorithm is given to screen out candidate agglomerates for mitigating the subsequent computation load, by defining an index to distinguish candidate agglomerates from all particles. By introducing two new texture descriptors for pattern recognition, a feature matching algorithm is proposed to recognize pseudo agglomeration. The number of primary particles involved in these agglomerates is counted by establishing a fast algorithm. The rock-like crystals of KDP as studied in the references^{21, 31} for image analysis are used for experimental tests to demonstrate the effectiveness of the proposed method for on-line detection.

For clarity, the paper is organized as follows. Section 2 briefly states the problem of detecting particle agglomeration. In Section 3, an image preprocessing method is presented to alleviate the influence from in-situ imaging conditions during the process operation. In Section 4, a preliminary sieving algorithm is given to screen out candidate agglomerates. A feature matching algorithm is proposed to recognize pseudo agglomerates in Section 5, along with an illustration on the advantage of the proposed texture descriptors compared to the existing image feature matching algorithms. Section 6 presents a fast algorithm to count the primary particles involved in the agglomerates. Experimental results are shown in Section 7 to demonstrate the effectiveness and advantage of the proposed method. Some conclusions are drawn in the last Section 8.

2. Problem of detecting particle agglomerates during crystallization

2.1 Double-view imaging system for monitoring a crystallizer

A non-invasive microscopic imaging system for monitoring industrial crystallization processes such as the KDP crystals grown from solution is shown in Figure 1. The imaging system including two

high-speed cameras made by Hainan Six Sigma Intelligent Systems Ltd was used to capture crystal images synchronously during the cooling crystallization process. The two cameras (UI-2280SE-C-HQ) with USB Video Class standard were made by IDS Imaging Development Systems GmbH, including two micro telescope lenses. The angle between these camera optic axes was set about 18 degrees to capture double-view images with two LED lights.

As shown in Figure 1, the crystallizer was composed of a 4-liter glass vessel, a 4-paddle agitator (PTFE), a thermostatic circulator (Julabo-CF41), and a temperature probe (PT100). Chemical compound used for the experiments was KDP (KH_2PO_4) with distilled water (H_2O) as solvent. The crystal suspension was monitored by the non-invasive microscopic double-view imaging system installed outside the vessel.

2.2 In-situ detection of particle agglomeration

In-situ image monitoring of particles in the suspension brings much more complexity compared to off-line image analysis of particles by using an optic microscopy. The major challenge lies in the fact that particle motion and solution turbulence in a stirred crystallizer provoke image blurring and additional noise. Secondly, the uneven light effect and time-varying hydrodynamics in the crystallizer interferes with the uniformity and intensity of the image background. In addition, there may be different gray scales between double-view images captured for the same particles, due to unequal distances from two camera lenses to the same particles. A typical scenario of double-view images is shown in Figure 2 by using the above imaging system.

It can be seen from the left view of Figure 2 that there possibly exists particle agglomeration. In fact, it can be verified from the right view of Figure 2 that the visual agglomerates were caused by particles overlapping in the left view. The phenomenon has been recognized as pseudo agglomeration in the literature. Herein the overlapped particles are defined by pseudo agglomerate for analysis. It is obvious that a single-view image, subject to lots of pseudo agglomerates, could mislead counting the crystal number and size, and thus affects on-line control and optimization of the crystal growth and product quality. Therefore, the recognition of pseudo agglomeration should be envisaged for on-line detection of the agglomeration degree. However, few methods were explored to solve this issue in the

literature, since the emergence of in-situ microscopic imaging technology for monitoring crystallization processes in the recent years^{3,8}.

To cope with the above problems, an in-situ image analysis method is proposed in this paper for detecting particle agglomeration during a crystallization process. The key idea is to recognize pseudo agglomerates by particle sieving and feature matching between double-view images. Correspondingly, the number of agglomerated particles can be efficiently counted. The agglomeration degree is evaluated by using the following specification³²,

$$P_A = \frac{N_{Ap}}{N_p} \times 100\% \quad (1)$$

where N_{Ap} is the number of primary particles involved in the agglomerates, N_p is the total number of valid particles counted in the image. Note that the primary particles means the recognized particles in these agglomerates, which originate from unagglomerated particles during the crystallization process. Correspondingly, the valid particles include these primary particles and unagglomerated particles detected in the captured image.

A flowchart of the proposed double-view image analysis method is shown in Figure 3. It can be seen that there are four steps for on-line implementation, including image preprocessing, preliminary sieving, feature matching, and particle counting, as detailed in the following sections, respectively.

3. Image preprocessing

3.1 Image reduction

For using a microscopic imaging system, the size of an image depends on the system resolution and the magnification of camera lens. A larger image size corresponds to a longer time delay for on-line analysis. An efficient image reduction method is therefore adopted to shrink the size of a captured image while maintaining fundamental image features to facilitate on-line analysis. Considering that the method has the advantage of high reduction ratio and good denoising ability, a two-dimensional discrete wavelet transform algorithm with the bi-orthogonal wavelet function³³ is constructed for a captured image denoted by $I(x, y)$ with a size of $M \times N$. Denoting by m the row, by n the column, and by j the number of decomposition levels, the low frequency component of discrete

wavelet transform for $I(x, y)$ is defined as

$$A(j, m, n) = \frac{1}{\sqrt{MN}} \sum_{x=1}^M \sum_{y=1}^N I(x, y) \varphi_{j,m,n}(x, y) \quad (2)$$

where

$$\varphi_{j,m,n}(x, y) = 2^{j/2} \varphi(2^j x - m, 2^j y - n) \quad (3)$$

Then the low frequency component $A(j, m, n)$ is used to approximate the original image $I(x, y)$.

As a result, a reduction image $f(x, y)$ is constructed from the low frequency component.

3.2 Image segmentation

To alleviate the influence from uneven image background, morphology processing is considered as an efficient approach based on the crystal shape characteristics. The uneven background is extracted by using an opening operation algorithm with the structuring element³⁴.

To properly parameterize the structuring element, a watershed transform algorithm³³ is used for computation. The watershed transform algorithm classifies catchment basins and watershed ridge lines in an image by treating it as a surface where light and dark pixels correspond to high and low values, respectively. The averaged distance between the watershed ridge lines is taken as a parameter of the structuring element. Then the uneven background is extracted by using the above algorithm.

Subsequently, the raw image is subtracted by the above uneven background. The segmentation threshold t^* is computed by using the Otsu thresholding function³³ as

$$t^* = \arg \max_t (\sigma^2(t)) \quad (4)$$

where $\sigma^2(t)$ is the variance between two gray level classes with a threshold value of $t \in [1, L]$ and L is the maximum gray level.

Finally, the segmented image is obtained by

$$q(x, y) = \begin{cases} 0, & f(x, y) < t^* \\ 1, & f(x, y) \geq t^* \end{cases} \quad (5)$$

After the segmentation, morphological region filling is performed to fill up all the holes inside the segmented image $q(x, y)$, such that the resulting image only remains all the particle regions while the image background is removed.

4. Preliminary sieving

This step is to screen out candidate agglomerates by using the particle shape features from the segmented double-view images, in order to save computation time for specifically recognizing pseudo agglomerates among these candidate agglomerates, while counting the number of valid particles in these images.

In fact, it remains open to describe the shape feature of particle agglomeration, though a few features describing particle shapes were explored in the literature^{8, 20}. In this work, the inner distance descriptor recently proposed in the reference¹⁴ is further extended to describe the agglomeration feature so as to sieve out the candidate agglomerates efficiently. The coordinates of particle boundary are denoted by (x_n, y_n) , $n=1, 2, \dots, N$, and the centroid coordinate (x_c, y_c) is denoted by

$$\begin{cases} x_c = \frac{1}{N} \sum_{n=0}^{N-1} x_n \\ y_c = \frac{1}{N} \sum_{n=0}^{N-1} y_n \end{cases} \quad (6)$$

The distances from the particle centroid to its boundary points are defined as

$$d_n = \sqrt{(x_c - x_n)^2 + (y_c - y_n)^2} \quad (7)$$

A deviation distance is defined by

$$\rho_n = d_n - \bar{d} \quad (8)$$

where \bar{d} is the mean value of d_n .

The curvature of ρ_n is computed by

$$c_n = \frac{\rho_n''}{(1 + \rho_n'^2)^{3/2}} \quad (9)$$

An index of the inner distance based curvature (IDC) is therefore proposed as

$$\text{IDC} = \frac{\sum_{n=1}^N c_n}{N} \quad (10)$$

For illustration, Figure 4 shows a few simplified round-like shapes of an unagglomerated particle and three agglomerates involved with two, three, and four particles, respectively. It is found that the IDC index of the single particle is evidently larger than the others, which may be used for recognizing

candidate agglomerates. Note that for rod-like and needle-like particle shapes, the corresponding IDC indices may be similar to those of the involved agglomerates, due to a relatively large length-width ratio of such a particle or agglomerate. Additional shape features, e.g., the specific elongation ratios and perimeters of different crystals, Fourier descriptors, and geometric moments as studied in the reference ¹⁴, may be adopted to further recognize candidate agglomerates.

Based on collecting typical shapes of individual particles and agglomerates in a crystallization process, the corresponding IDC indices are constructed as a training set for preliminary sieving. By classifying all the IDC indices into two groups, one for candidate agglomerates and the other for unagglomerated particles, a linear classification algorithm is established below.

Denote by \mathbf{a}_1 and \mathbf{a}_2 for the IDC index groups of candidate agglomerates and unagglomerated particles, respectively. The central value u_i of \mathbf{a}_i ($i=1,2$) is computed by

$$u_i = \arg \min_{u_i} \sum \|\mathbf{a}_i - u_i\|^2, \quad i=1,2 \quad (11)$$

The threshold t_0 for classification is determined by

$$t_0 = \frac{u_1 + u_2}{2} \quad (12)$$

To determine whether a segmented image region with an IDC index of b belongs to an agglomerate, a classification rule is proposed as follows:

$$b \in \begin{cases} \text{CA1, if } b \leq t_0; \\ \text{CA2, if } b > t_0. \end{cases} \quad (13)$$

where CA1 denotes the candidate agglomerate set and CA2 indicates the unagglomerated particle set.

5. Feature matching

To further recognize the pseudo agglomerates from the candidate agglomerates, an enhanced feature matching algorithm is proposed to procure accurate recognition, by establishing the image interest point location and its feature descriptors as developed in the references ²²⁻²⁵. For clarity, Figure 5 shows the flowchart of the feature matching process. Note that the raw surfaces of particles in the segmented double-view images are wholly stuffed within their contours before proceeding with the matching algorithm.

5.1 Interest point location

The Hessian matrix studied in SURF²⁴ is used for detecting the interest point location. Given an image point $Q(x, y)$, the Hessian matrix $H(Q, \sigma)$ in X is defined as

$$H(Q, \sigma) = \begin{bmatrix} L_{xx}(Q, \sigma) & L_{xy}(Q, \sigma) \\ L_{xy}(Q, \sigma) & L_{yy}(Q, \sigma) \end{bmatrix} \quad (14)$$

where $L_{xx}(Q, \sigma)$ is the convolution of the Gaussian second order derivative $\frac{\partial^2}{\partial x^2} g(\sigma)$ with respect to the image point Q , and so is for $L_{xy}(Q, \sigma)$ and $L_{yy}(Q, \sigma)$, σ is a parameter of the Gaussian function $g(\sigma)$, which denotes the image scale²².

To simplify the above computation, box filters are used instead of the Gaussian second order derivatives. Denoting D_{xx} , D_{yy} and D_{xy} as the approximations of the Gaussian second order derivatives for each image by using the box filters, respectively, an approximation determinant of the Hessian matrix can be written as

$$\text{Det}(H) = D_{xx}D_{yy} - (0.9D_{xy})^2 \quad (15)$$

The scale space is described as an image pyramid, which is divided into 4 octaves, and each octave includes 4 levels together with box filters of different window sizes denoted by L . By using the integral image, the local maxima as a candidate interest point may be selected in a $3 \times 3 \times 3$ neighborhood in the scale space, such that the convolution computation could be accelerated²⁴.

For using the box filters, the parameters cannot be chosen arbitrarily. Following the guideline in the reference³⁵, it is preferred to take

$$\begin{cases} L = 2^o \times i + 1 \\ \sigma = \frac{1.2}{3} L \end{cases} \quad (16)$$

where $o \in \{1, 2, 3, 4\}$ is the octave index and $i \in \{1, 2, 3, 4\}$ is the level index.

Moreover, a distance constraint is additionally imposed in the same scale σ to avoid the interest points over dense in a local area, because the density affects the matching efficiency. For example, denoting Ψ as the interest point set, a distance-constrained rule is defined for two interest points $X(x_1, y_1)$ and $X(x_2, y_2)$ as

$$\begin{cases} X(x_1, y_1) \in \Psi, & \text{if } \text{Dis} < \lambda \text{ and } R(x_1, y_1) - R(x_2, y_2) \geq 0; \\ X(x_2, y_2) \in \Psi, & \text{if } \text{Dis} < \lambda \text{ and } R(x_1, y_1) - R(x_2, y_2) < 0; \\ X(x_1, y_1) \text{ and } X(x_2, y_2) \in \Psi, & \text{if } \text{Dis} \geq \lambda. \end{cases} \quad (17)$$

where $\text{Dis} = (x_1 - x_2)^2 + (y_1 - y_2)^2$, $R(x_1, y_1)$ and $R(x_2, y_2)$ denote gray levels, and λ is a distance threshold similar to the parameter of the structuring element in Section 3.2.

5.2 Feature descriptor

The Haar wavelet responses in SURF²⁴, which can be quickly computed via integral images, are used to construct a feature descriptor. Firstly, the dominant orientation of the Haar descriptor for the interest point is computed by detecting the longest vector of the summed Gaussian weighted Haar wavelet responses under a sliding sector window of $\pi/3$.

To determine the descriptor, a square region is chosen around the interest point. The region is split into smaller 4×4 square sub-regions. For each sub-region, the Haar wavelet response dx perpendicular to the dominant orientation and the Haar wavelet response dy in the dominant orientation are computed. Hence, a four-dimensional (4D) Haar descriptor, $(\sum dx, \sum |dx|, \sum dy, \sum |dy|)$, is established for each sub-region. Given 4×4 square sub-regions for each interest point, a Haar descriptor of 64 dimensions denoted by v_H is subsequently constructed after normalization.

To compensate for the deficiency of the above descriptor in dealing with image noise and uneven illumination background, two texture descriptors are supplemented to enhance the matching accuracy for double-view images with high feature similarity. Inspired by the LBP approach developed in the references²⁷⁻³⁰, a deviation compensated LBP (DCLBP) descriptor and a magnitude difference based LBP (MDLBP) descriptor are proposed to improve the accuracy of describing the interest region in the presence of uneven illumination while mitigating the computation effort.

Denoting g_c as the gray value of the center pixel (i, j) in a local region, and g_p ($p = 0, \dots, P-1$) as the gray values of equally spaced P pixels in a circle of radius R with respect to the center pixel (i, j) , the location parameter g_a is defined as

$$g_a = \begin{cases} g_c - \text{std}_{P,R}, & \text{if } g_c \geq 1/(P+1) \sum_{p=1}^P (g_p + g_c); \\ g_c + \text{std}_{P,R}, & \text{if } g_c < 1/(P+1) \sum_{p=1}^P (g_p + g_c). \end{cases} \quad (18)$$

where $\text{std}_{P,R}$ is the standard deviation of gray value with respect to g_c and its neighborhood g_p .

Thus, the DCLBP for $G(i, j)$ is obtained as

$$\text{DCLBP}_{P,R}(i, j) = \sum_{p=1}^P s(g_p - g_a) 2^p \quad (19)$$

where

$$s(g_p - g_a) = \begin{cases} 1, & \text{if } g_p - g_a \geq T; \\ 0, & \text{if } g_p - g_a < T. \end{cases} \quad (20)$$

where T is a practically specified difference threshold, e.g., e^{-3} .

Considering that the magnitude information is also important for local texture structure description²⁸, we define the magnitude difference by $m_p = |g_c - g_p|$. Note that the vector $[m_0, m_1, \dots, m_{p-1}]$ is less sensitive to uneven illumination, which is therefore transformed into the binary pattern for analysis. Correspondingly, the MDLBP is obtained as

$$\text{MDLBP}_{P,R}(i, j) = \sum_{p=1}^P (s_p - \overline{m}_p) 2^p \quad (21)$$

where \overline{m}_p is the averaged value for $[m_0, m_1, \dots, m_{p-1}]$, and

$$s(m_p - \overline{m}_p) = \begin{cases} 1, & \text{if } m_p - \overline{m}_p \geq T \\ 0, & \text{if } m_p - \overline{m}_p < T \end{cases} \quad (22)$$

For illustration, a numerical example studied in the reference³⁰ is performed here to demonstrate the proposed texture recognition of image micro-structure. Figure 6 shows three texture patterns with different features to classify and each of the patterns has the same center pixel with 8 neighbors. It is obvious that LBP and the proposed DCLBP have different thresholds in terms of the same $P = 8$. The three patterns (a, b, c) are classified into the same pattern by using LBP, due to the oversimplified local structure recognized by LBP. By introducing a complementary feature, called VAR, which could reflect the local contrast of each pattern, The reference²⁶ proposed the combination of VAR and LBP for recognition, as shown in Figure 6 (ii) and (iii). It can be seen that the patterns (a) and (b) can be distinguished but the patterns (b) and (c) are still regarded as the same texture, due to neglecting the differences between the center and each neighbor. In contrast, both of the proposed DCLBP and MDLBP have effectively recognized different binary patterns for these three texture patterns, as shown in Figure 6 (iv) and (v), owing to further detailed description of local texture feature in the interest region.

Moreover, taking into account the rotation invariance of LBP²⁶, we denote $DCLBP_{P,R}^{Ri}(i, j)$ and $MDLBP_{P,R}^{Ri}(i, j)$ as the rotation invariants of DCLBP and MDLBP, respectively. Distribution histograms of the DCLBP and MDLBP values are taken as two dimensions in the feature descriptor. The property of the histogram may facilitate analyzing the statistical region characteristics and reducing the pattern dimension²⁹. Take the DCLBP as an example, in the interest region $N \times N$ for the interest point, the DCLBP value of each pixel point $G(i, j)$ is computed to generate the DCLBP spectrogram composed of $DCLBP_{P,R}^{Ri}(i, j)$, $i, j = 1, 2, \dots, N$. Therefore, the interest region is represented by a one-dimensional pattern histogram²⁹ as

$$h(k) = \sum_{i=1}^N \sum_{j=1}^N f(DCLBP_{P,R}^{Ri}(i, j), k), \quad k \in [0, K] \quad (23)$$

where K is the maximal DCLBP pattern value, and

$$f(DCLBP_{P,R}^{Ri}(i, j), k) = \begin{cases} 1, & \text{if } DCLBP_{P,R}^{Ri}(i, j) = k; \\ 0, & \text{if } DCLBP_{P,R}^{Ri}(i, j) \neq k. \end{cases} \quad (24)$$

Then, the texture feature vector v_D is determined by normalizing $h(k)$, $k \in [0, K]$. Note that the dimension of v_D is determined by the interest region size, which is suggested to be $\sqrt{2}N$ based on numerical computation. Similar to v_D , the MDLBP feature vector denoted by v_M can be determined.

Besides, the feature of dominant orientation²⁵ is also considered in the DCLBP spectrogram, which is denoted by $L(i, j)$. Define the main orientation being from the interest point to the centroid ($\bar{i} = \sum i \cdot L(i, j) / \sum L(i, j)$, $\bar{j} = \sum j \cdot L(i, j) / \sum L(i, j)$). Denoting by Ω_{mo} all the point set in the main orientation, $L(m, n)$ ($m, n \in \Omega_{mo}$) is decomposed by the discrete Fourier transform. A weighted amplitude $v_{aw}(m, n)$ is defined by

$$v_{aw}(m, n) = \omega(m, n) \cdot v_a(m, n) \quad (25)$$

where $v_{am}(m, n)$ is the amplitude of $L(m, n)$ in the Fourier transform, and

$$\omega(m, n) = \frac{1}{2\pi\sigma^2} e^{\frac{-r^2}{2\sigma^2}} \quad (26)$$

where r is the distance between the pixel $DCLBP_{P,R}^{Ri}(m, n)$ and the interest point, and σ is the image scale of the interest point.

Correspondingly, the feature of dominant orientation v_o is taken as the mean of v_{am} after normalization.

To sum up, the interest point descriptor is composed of $v = [v_H \ v_D \ v_M \ v_O]$.

5.3 Descriptor matching

The above interest point descriptor generally has high dimension, which may be inefficient and computationally intensive for matching. Hence, dimension reduction is adopted to improve computation efficiency. The idea of linear graph embedding (LGE) with locality preserving projection (LPP) ³⁶ is adopted herein to extract the geometric features and local region characteristics. For a pair of double-view images, the interest point descriptor set is defined by $V = \{v_1, \dots, v_n\}$, $v_i \in \mathbb{R}^m$, where m is the dimension of the interest point descriptor and n is the number of the interest point. The interest point descriptor is depicted by an undirected graph G with n vertices, while each vertex indicates an interest point denoted by v_i . To evaluate the similar degree of different interest points, a symmetric matrix W is defined with the elements denoted by w_{ij} which is the weight of the edge from the vertex v_i to the vertex v_j .

$$w_{ij} = \begin{cases} e^{-\|v_i - v_j\|^2 / \tau^2}, & \text{if } v_i \in N_k(v_j) \text{ or } v_j \in N_k(v_i); \\ 0, & \text{if } v_i \notin N_k(v_j) \text{ and } v_j \notin N_k(v_i). \end{cases} \quad (27)$$

where $N_k(v_i)$ denotes the set of the k -nearest neighbors of v_i with a choice of $k=5$ herein for computation, and τ is the averaged Euclidean distance among these points.

Let $B = [b_1, \dots, b_n]^T$ be a map from the graph to a real line. The optimal B is determined by

$$\min \sum_{i,j} (b_i - b_j)^2 w_{ij} \quad (28)$$

It can be derived from (28) that

$$\frac{1}{2} \sum_{i,j} (b_i - b_j)^2 w_{ij} = B^T L B \quad (29)$$

where $L = D - W$ is the graph Laplacian, D a diagonal matrix whose entries are column (or row) sums of W , $d_{ii} = \sum_j w_{ji}$.

A minimization programming is established for solving (29) by

$$\arg \min B^T L B \quad \text{s.t. } B^T D B = 1 \quad (30)$$

The LGE is used to establish a linear approximation for the nonlinear relationship, $b_i^T = v_i^T U$, where U is a projection matrix. After simplification, the optimal U is given by the minimum eigenvalue of the generalized eigenvector for the following equation,

$$V L V^T U = \lambda V D V^T U \quad (31)$$

Note that if the number of descriptor samples is small for dimension reduction, the matrix $V^T L V$ may be singular. It is therefore proposed to project the sample set into the PCA space³⁶ in advance.

However, the computation load could become very heavy if using the global nearest neighbor searching method²⁴ to reduce the descriptor dimension for the interest points between the double-view images. It is therefore proposed to use the approximately nearest neighbor searching algorithm via the K-dimension (KD) tree³⁷ to save the computation effort.

Meanwhile, considering that the interest point descriptors could be mismatched if the scale difference is large, it is proposed to limit the scale difference for feature matching, that is, the scale difference S_{di} of interest point pairs should satisfy

$$S_{di} \leq \bar{S} + W_s \quad (32)$$

where \bar{S} is the averaged scale value for all the interest points, and W_s is the scale standard deviation.

To ensure the matching accuracy and stability, an outlier detection algorithm is proposed to remove outliers in the matching points. By denoting (x_1, y_1) and (x_2, y_2) as two matching points, the angle a between them is defined as

$$a = \arctan \frac{y_2 - y_1}{x_2 - x_1} \quad (33)$$

Denoting $A = \{a(i) | i = 1, 2, \dots, m\}$ as the angle set, where m is the number of matching points, $N(j)$ as the number in the cluster j , and $\mu(j)$, $j = 1, \dots, k$ as the cluster centroids computed from A , where j is the cluster index number, the k -means clustering algorithm³⁸ is performed by iterating the following two steps until $\mu(j)$ converges to the optimum, with an initially random choice of $\mu(j)$ within A .

Firstly, assign $a(i)$ into the nearest cluster of $c(i)$ defined by

$$c(i) = \arg \min_j \|a(i) - \mu(j)\|^2 \quad (34)$$

Secondly, update the cluster centroids $\mu(j)$ ($j = 1, \dots, k$) of A by

$$\mu(j) = \frac{\sum_{i=1}^m 1\{c(i) = j\} a(i)}{\sum_{i=1}^m 1\{c(i) = j\}}, \quad j = 1, \dots, k \quad (35)$$

After clustering, the minimum number of j^* is obtained as

$$j^* = \arg \min_j N(j), \quad j = 1, \dots, k \quad (36)$$

Then all the matching points within the corresponding angle cluster of j^* are classified as candidate outliers. Let u_o be the mean value of the original angle set and u_r the mean value of the angle set excluding j^* . If $|u_r - u_o| \geq \pi/60$, the optimized matching is selected by deleting the candidate outliers. Otherwise, these candidate outliers should be remained.

After outlier detection, a label processing is proposed to recognize pseudo agglomerates. Firstly, all particles in the segmented images are labeled. If there is one-to-one relationship between two matching labels respectively in the double-view images, they should be recognized as agglomerated particles. Otherwise, the candidate agglomerates should be viewed as pseudo agglomerates.

6. Particle counting

For pseudo agglomerates, the corresponding particles can be easily counted by using the one-to-many relationship of label processing. However, for true agglomerates, it remains difficult to count the number of primary particles involved in these agglomerates. By virtue of the analysis on IDC as shown in Figure 4, it is proposed to use the concave points of the agglomerate contours to count the primary round-like particles in these agglomerates. A fast algorithm is therefore given as illustrated in Figure 7, based on the morphology mask as follows.

Step 1. A toolbox algorithm³³ is used to figure out the convex hull (S_{ch}) for a true agglomerate, while the contour of S_{ch} is entirely stuffed.

Step 2. The concavities (S_{co}) are computed as the difference between the convex hull (S_{ch}) and the agglomerate (S_{ag}), i.e., $S_{co} = S_{ch} - S_{ag}$.

Step 3. The value of saliency $Sal(b)$ is calculated for the boundary point b in the contour image by

$$Sal(b) = \frac{M_b}{M_{ci}} \quad (37)$$

where M_{ci} is the pixel number of the circle mask centered on the boundary b , and M_b is the number of pixels in the maximum background block in the circle mask M . The mask center b scans over the boundary of the contour by using a circle mask M with radius R_p . Saliency points are located in terms of $Sal(b) \geq 0.7$. If several continuous points comply with the condition, the point corresponding to the largest $Sal(b)$ is taken as a saliency point.

Step 4. A concave point on the agglomerate boundary is determined if all the connecting lines between the concave point and its adjacent salience points are inside the agglomerate.

Step 5. By drawing the nearest connecting lines between the determined concave points in different concavities while avoiding any closed loop possibly constructed by the connecting lines, the number of primary particles involved in these agglomerates is counted as the number of these connecting lines plus one.

7. Experimental results

A seeded KDP cooling crystallization experiment was performed to verify the effectiveness of the proposed image analysis method for recognizing pseudo agglomerates. The KDP solution was firstly heated up to 40 °C and maintained at the temperature for an hour to ensure complete dissolution of the solute. Then the solution was cooled down with a cooling rate of 0.3°C/min. The crystal seeds were added shortly after the solution went into the supersaturated zone. The agitator was operated at a speed of 150 rpm to keep all particles in suspension during the cooling crystallization process for image monitoring. The aforementioned non-invasive microscopic imaging system was applied for in-situ imaging, by using two LED lights with an illumination level of 400lux. In the double-view imaging system, each image was taken at the pixel resolution of 2448×2048 per second. Note that 30 particles were chosen from the previously captured images as the IDC training set to establish the classification rule of preliminary sieving in advance.

Considering the in-situ captured double-view images shown in Figure 2, the image analysis method is illustrated in Figure 8. Firstly, the preprocessed images are shown in Figure 8 (a) by using the reduction approach presented in Section 3. Then Figure 8 (b) shows the result by removing the image background. Figure 8 (c) shows the segmented double-view image where the particle intensity and the background are denoted by 1 and 0, respectively. Note that each pairs of double-view images were simultaneously processed throughout the proposed analysis procedure. Figure 8 (d) shows the candidate agglomerate recognized by the preliminary sieving using the IDC indices as listed in the figure. Subsequently, Figure 8 (e) shows the pseudo agglomerate recognized by using the proposed feature matching algorithm where the parameters of DCLBP and MDLBP were taken as $P=8$ and

$R = 2$. Note that all the valid particles and interest points were rightly matched between the double-view images.

To compare the matching performance for the in-situ double-view images captured during the crystallization process, the developed algorithms, SIFT²², ASIFT²³, SURF²⁴ and ORB²⁵, were also performed for Figure 2 based on the above image preprocessing and preliminary sieving. The parameter of Gaussian function in SIFT and ASIFT was taken as 1.6, the parameters of SURF were computed in terms of (16) in Section 5, and the parameters of ORB were chosen with the radius of neighborhood being 3 and the edge threshold being 31, according to the guidelines given therein. Note that the proposed outlier detection algorithm was performed beforehand to perform these algorithms for fair comparison. The matching results are shown in Figure 9. It is seen that none of these algorithms could give perfect matching for all the particles including the agglomerate. Figure 9 (a) shows that SIFT gives correct matching for most of the interest points as shown in Figure 8 (e), but a prominent interest point was overlooked as indicated by the yellow circle. In Figure 9 (b), it is obvious that a valid particle was not matched in the double-view images by using ASIFT. Figure 9 (c) shows that there is a mismatch of an interest point by using SURF, as indicated by the red line. Figure 9 (d) shows that a valid particle is not matched while there exists a mismatch of an interest point (indicated by the purple line) by using ORB.

To further demonstrate the effectiveness of the proposed algorithm for recognizing particle agglomeration and counting the number of primary particles, Figure 10 shows the imaging analysis results for another pair of double-view images captured from the crystallization process, which includes true agglomeration. It is seen from Figure 10 (b) that the candidate agglomerates were recognized by using the preliminary sieving step, as indicated by the red contours. Then it is verified in Figure 10 (c) by using the proposed feature matching algorithm that there are two agglomerates in the left view. From Figure 10 (d) it is seen that the number of the primary particles involved in the agglomerates is properly counted by the proposed algorithm.

Table 1 lists the recognition results for two different cases shown in Figure 8 and Figure 10, respectively, for pseudo and true agglomerates. It can be seen that the proposed image analysis method can give precise assessment on the agglomeration degree and the total number of particles, while the

number of unagglomerated particles and the number of primary particles involved in the agglomerates are rightly counted, respectively.

In addition, to demonstrate the effectiveness of the proposed method for on-line monitoring the crystallization process, thirty pairs of double-view images including more than 200 particles captured from the crystallization experiment, as illustrated in Figure 11 (including 6 representative pairs of double-view images taken at different time instants), were taken to verify the proposed feature matching algorithm in comparison with the above algorithms. For 6 representative pairs of these images, the agglomeration degree defined in (1) is evaluated by using the proposed double-view analysis, which is denoted by P_{A-2} in Figure 11. For comparison, the corresponding result given by using the single-view analysis method^{18,20} is denoted by P_{A-1} in Figure 11. It is seen that the proposed double-view analysis gives proper assessment of the agglomeration degree in real time (made per 5 minutes during the crystallization process), compared to the single-view analysis that gives obvious misestimate such as the result for the image taken at the moment denoted by (15-20min). In other words, the real-time estimation error arising from particle overlapping is significantly reduced by using the proposed double-view analysis.

To evaluate the matching effect, the particle recall ratio P_{pr} is defined by

$$P_{pr} = \frac{N_{pa}}{N_{pa} + N_{pm}} \quad (38)$$

where N_{pa} is the number of matched particles and N_{pm} is the number of unmatched particles.

The matching accuracy of interest points is defined by

$$P_{pm} = \frac{N_a}{N_t} \quad (39)$$

where N_a is the number of correct point matches and N_t is the total number of point matches. Note that a valid particle is recognized if the point matching for two double-view images of the particle is over 80%.

Three indices including point matching accuracy, particle recall ratio and averaged computation time per frame were computed for comparison as listed in Table 2. Note that all of the above algorithms used the same global nearest neighbor searching method²⁴ for computation. It is seen in Table 2 that the proposed algorithm gave the best point matching accuracy and the highest particle recall ratio while

using a moderate computation time for each frame of double-view images. In contrast, SIFT and ASIFT gave similar point matching accuracy close to that of the proposed algorithm. However, they required an evidently longer computation time compared to the proposed algorithm, due to the use of high-dimensional feature descriptors. Although ORB spent the shortest computation time in these algorithms, the resulting point matching accuracy and particle recall ratio were the lowest compared to the other algorithms, due to insufficient description of local features. By using a computation time similar to the proposed algorithm, SURF gave inferior point matching accuracy, by using less local texture features compared to the proposed algorithm. Note that for monitoring the crystallization process, the particle recall ratio reflecting particle matching is more important than the other two indices for agglomerate recognition. The result in Table 2 well demonstrates that the proposed algorithm can give good matching and recognition for on-line monitoring particle agglomeration.

8. Conclusions

Based on an in-situ installed double-view imaging system, a synthetic image analysis method has been proposed in this paper for monitoring particle agglomeration during a crystallization process. A fast image segmentation approach based on image reduction is firstly adopted to perform image preprocessing so as to reduce the influence from uneven illumination background and solution turbulence. By defining an IDC index to detect possible agglomeration, a preliminary sieving algorithm is given to screen out candidate agglomerates from preprocessed images, effectively mitigating the on-line computation load. Then by introducing two texture descriptors, DCLBP and MDLBP, for pattern recognition, a fast feature matching algorithm is developed to recognize pseudo agglomerates with good accuracy. Subsequently, an efficient particle counting algorithm is established to assess the agglomeration degree, by which both the unagglomerated particles and the primary particles involved in agglomerates can be precisely counted, respectively. Experimental tests on monitoring the KDP crystallization process well demonstrate that the proposed strategy can be more effectively used for monitoring the crystal agglomeration degree in comparison with the existing single-view analysis, along with obvious superiority for particle matching between double-view images compared to the developed image feature matching methods.

Acknowledgment

This work was supported in part by the NSF China Grant 61633006 and the National Thousand Talents Program of China.

References

- (1) Li, M.; Wilkinson, D.; Patchigolla, K., Determination of non-spherical particle size distribution from chord length measurements. Part 2: Experimental validation. *Chemical Engineering Science* **2005**, 60, (18), 4992-5003.
- (2) Yu, Z.; Chew, J.; Chow, P.; Tan, R., Recent advances in crystallization control: an industrial perspective. *Chemical Engineering Research and Design* **2007**, 85, (7), 893-905.
- (3) Nagy, Z. K.; Fevotte, G.; Kramer, H.; Simon, L. L., Recent advances in the monitoring, modelling and control of crystallization systems. *Chemical Engineering Research and Design* **2013**, 91, (10), 1903-1922.
- (4) Zhang, B.; Willis, R.; Romagnoli, J. A.; Fois, C.; Tronci, S.; Baratti, R., Image-based multiresolution-ANN approach for online particle size characterization. *Industrial & Engineering Chemistry Research* **2014**, 53, (17), 7008-7018.
- (5) Schorsch, S.; Ochsenein, D. R.; Vetter, T.; Morari, M.; Mazzotti, M., High accuracy online measurement of multidimensional particle size distributions during crystallization. *Chemical Engineering Science* **2014**, 105, (2), 155-168.
- (6) Zhou, Y.; Srinivasan, R.; Lakshminarayanan, S., Critical evaluation of image processing approaches for real-time crystal size measurements. *Computers & Chemical Engineering* **2009**, 33, (5), 1022-1035.
- (7) Li, P.; He, G.; Lu, D.; Xu, X.; Chen, S.; Jiang, X., Crystal size distribution and aspect ratio control for rodlike urea crystal via two-dimensional growth evaluation. *Industrial & Engineering Chemistry Research* **2017**, 56, (9), 2573-2581.
- (8) Wang, X. Z.; Roberts, K. J.; Ma, C., Crystal growth measurement using 2D and 3D imaging and the perspectives for shape control. *Chemical Engineering Science* **2008**, 63, (5), 1173-1184.
- (9) Zhou, Y.; Lakshminarayanan, S.; Srinivasan, R., Optimization of image processing parameters for large sets of in-process video microscopy images acquired from batch crystallization processes: Integration of uniform design and simplex search. *Chemometrics & Intelligent Laboratory Systems* **2011**, 107, (2), 290-302.
- (10) Schorsch, S.; Vetter, T.; Mazzotti, M., Measuring multidimensional particle size distributions during crystallization. *Chemical Engineering Science* **2012**, 77, (1), 130-142.
- (11) Chen, X.; Zhou, W.; Cai, X.; Su, M.; Liu, H., In-line imaging measurements of particle size, velocity and concentration in a particulate two-phase flow. *Particuology* **2014**, 13, (2), 106-113.
- (12) Zhang, R.; Ma, C. Y.; Liu, J. J.; Wang, X. Z., On-line measurement of the real size and shape of crystals in stirred tank crystalliser using non-invasive stereo vision imaging. *Chemical Engineering Science* **2015**, 137, (10), 9-21.
- (13) Larsen, P. A.; Rawlings, J. B., The potential of current high-resolution imaging-based particle size distribution measurements for crystallization monitoring. *AIChE Journal* **2009**, 55, (4), 896-905.
- (14) Huo, Y.; Liu, T.; Liu, H.; Ma, C. Y.; Wang, X. Z., In-situ crystal morphology identification using imaging analysis with application to the L-glutamic acid crystallization. *Chemical Engineering Science* **2016**, 148, (12), 126-139.
- (15) Zhang, R.; Ma, C. Y.; Liu, J. J.; Zhang, Y.; Liu, Y. J.; Wang, X. Z., Stereo imaging camera model for 3D shape reconstruction of complex crystals and estimation of facet growth kinetics. *Chemical Engineering Science* **2017**, 160, 171-182.
- (16) Ulrich, J.; Froberg, P., Problems, potentials and future of industrial crystallization. *Frontiers of Chemical Science and Engineering* **2013**, 7, (1), 1-8.
- (17) Ålander, E. M.; Uusi-Penttilä, M. S.; Rasmuson, Å. C., Characterization of paracetamol agglomerates by image analysis and strength measurement. *Powder Technology* **2003**, 130, (1), 298-306.
- (18) Ferreira, A.; Faria, N.; Rocha, F.; Teixeira, J., Using an online image analysis technique to characterize sucrose crystal morphology during a crystallization run. *Industrial & Engineering Chemistry Research* **2011**, 50, (11), 6990-7002.

- (19) Terdenge, L. M.; Heisel, S.; Schembecker, G.; Wohlgemuth, K., Agglomeration degree distribution as quality criterion to evaluate crystalline products. *Chemical Engineering Science* **2015**, 133, (8), 157-169.
- (20) Ochsenbein, D. R.; Vetter, T.; Schorsch, S.; Morari, M.; Mazzotti, M., Agglomeration of needle-like crystals in suspension: I. Measurements. *Crystal Growth & Design* **2015**, 15, (4), 1923-1933.
- (21) Borchert, C.; Temmel, E.; Eisenschmidt, H.; Lorenz, H.; Seidelmorgenstern, A.; Kai, S., Image-based in situ identification of face specific crystal growth rates from crystal populations. *Crystal Growth & Design* **2014**, 14, (3), 952-971.
- (22) Lowe, D. G., Distinctive image features from scale-invariant keypoints. *International Journal of Computer Vision* **2004**, 60, (2), 91-110.
- (23) Morel, J. M.; Yu, G., ASIFT: A new framework for fully affine invariant image comparison. *Siam Journal on Imaging Sciences* **2009**, 2, (2), 438-469.
- (24) Bay, H.; Ess, A.; Tuytelaars, T.; Gool, L. V., Speeded-up robust features (SURF). *Computer Vision & Image Understanding* **2008**, 110, (3), 346-359.
- (25) Rublee, E.; Rabaud, V.; Konolige, K.; Bradski, G. In ORB: An efficient alternative to SIFT or SURF, *International Conference on Computer Vision*, 2011; 2011; pp 2564-2571.
- (26) Ojala, T.; Pietikäinen, M.; Mäenpää, T., Multiresolution gray-scale and rotation invariant texture classification with local binary patterns. *IEEE Transactions on Pattern Analysis & Machine Intelligence* **2002**, 24, (7), 971-987.
- (27) Liu, L.; Fieguth, P.; Guo, Y.; Wang, X.; Pietikäinen, M., Local binary features for texture classification: Taxonomy and experimental study. *Pattern Recognition* **2017**, 62, 135-160.
- (28) Guo, Z.; Zhang, L.; Zhang, D., A completed modeling of local binary pattern operator for texture classification. *IEEE Transactions on Image Processing* **2010**, 19, (6), 1657-63.
- (29) Guo, Z.; Zhang, L.; Zhang, D., Rotation invariant texture classification using LBP variance (LBPV) with global matching. *Pattern Recognition* **2010**, 43, (3), 706-719.
- (30) Liu, L.; Zhao, L.; Long, Y.; Kuang, G.; Fieguth, P., Extended local binary patterns for texture classification. *Image & Vision Computing* **2012**, 30, (2), 86-99.
- (31) Yang, G.; Kubota, N.; Sha, Z.; Louhi-kultanen, M.; Wang, J., Crystal shape control by manipulating supersaturation in batch cooling crystallization. *Crystal Growth & Design* **2006**, 6, (12), 2799-2803.
- (32) Nývlt, J.; Karel, M., Crystal agglomeration. *Crystal Research and Technology* **1985**, 20, (2), 173-178.
- (33) Gonzales, R. C.; Woods, R. E.; Eddins, S. L., *Digital image processing using MATLAB*. Pearson Prentice Hall: Upper Saddle River, NJ, 2004.
- (34) Chen, J.; Wang, X. Z., A wavelet method for analysis of droplet and particle images for monitoring heterogeneous processes. *Chemical Engineering Communications* **2005**, 192, (4), 499-515.
- (35) Oyallon, E.; Rabin, J., An analysis of the SURF method. *Image Processing On Line* **2015**, 5, (337), 176-218.
- (36) Cai, D.; He, X.; Han, J. In Spectral regression for efficient regularized subspace learning, *International Conference on Computer Vision*, 2007; 2007; pp 1-8.
- (37) Arya, S.; Mount, D. M.; Netanyahu, N. S.; Silverman, R.; Wu, A. In An optimal algorithm for approximate nearest neighbor searching, *Acm-Siam Symposium on Discrete Algorithms*. 23-25 January 1994, Arlington, Virginia, 1994; 1994; pp 573-582.
- (38) Jain, A. K.; Myrthy, M. N.; Flynn, P. J.; Jain, A. K.; Myrthy, M. N., Data clustering: A survey. *Acm Computing Survey* **1999**, 31, (2), 264-323.

List of Table and Figure Captions

Table 1. Recognition results for two different cases

Table 2. Comparison of matching results by using different algorithms

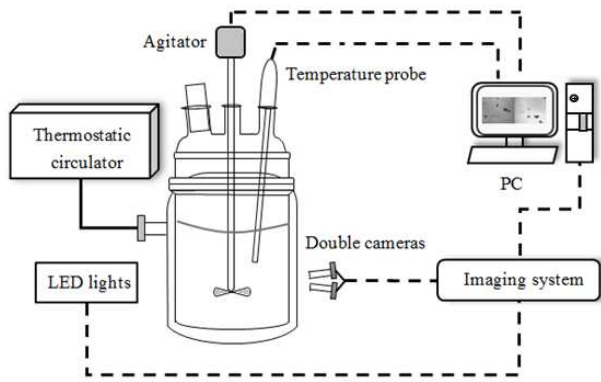
- Figure 1.** (a) Schematic of a microscopic image monitoring system for crystallization monitoring; (b) Experimental set-up of a non-invasive microscopic double-view imaging system
- Figure 2.** In-situ double-view images captured by a microscopic imaging system
- Figure 3.** Flowchart of the proposed method for agglomeration detection
- Figure 4.** Illustration of IDC: (a) an unagglomerated particle; (b) agglomerate of two particles; (c) agglomerate of three particles; (d) agglomerate of four particles
- Figure 5.** Flowchart of the proposed feature matching algorithm
- Figure 6.** Comparison of texture recognition: (i) three different texture patterns (a, b, c); (ii) LBP (a1, b1, c1); (iii) VAR values (a2, b2, c2); (iv) DCLBP (a3, b3, c3); (v) MDLBP (a4, b4, c4)
- Figure 7.** Schematic of the proposed counting algorithm for particle agglomeration
- Figure 8.** Double-view image processing for in-situ captured images: (a) preprocessed images; (b) result after removing the background; (c) segmented result; (d) preliminary sieving with IDC (a candidate agglomerate is labeled in red contour); (e) feature matching (the candidate agglomerate in the left view corresponds to two particles in the right view)
- Figure 9.** Comparison of matching results: (a) SIFT; (b) ASIFT; (c) SURF; (d) ORB
- Figure 10.** Agglomerate recognition and particle counting results: (a) in-situ captured double-view images; (b) preliminary sieving (candidate agglomerates are labeled with red contour); (c) feature matching; (d) counting primary particles in the agglomerates (the connecting lines indicating four primary particles in the two agglomerates in the left view)
- Figure 11.** Microscopic double-view images captured during the KDP crystallization process

Table 1. Recognition results for two different cases

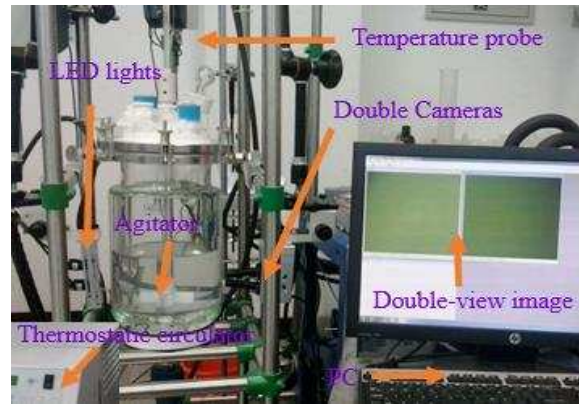
| Target parameters in the double-view images | Case 1 | Case 2 |
|--|---------------|---------------|
| The number of pseudo agglomerates | 1 | 0 |
| The number of true agglomerates | 0 | 2 |
| The number of unagglomerated particles | 5 | 3 |
| The number of primary particles involved in the agglomerates | 0 | 4 |
| The total number of all the primary particles | 5 | 7 |
| The agglomeration degree | 0% | 57.14% |

Table 2. Comparison of matching results by using different algorithms

| Methods | Particle recall ratio (%) | Point matching accuracy (%) | Averaged computation time per frame (s) |
|----------------|----------------------------------|------------------------------------|--|
| Proposed | 97.96 | 92.01 | 0.9347 |
| SIFT | 94.90 | 91.83 | 1.3703 |
| ASIFT | 93.88 | 91.65 | 1.8061 |
| SURF | 95.92 | 88.47 | 0.8925 |
| ORB | 90.82 | 83.95 | 0.4126 |

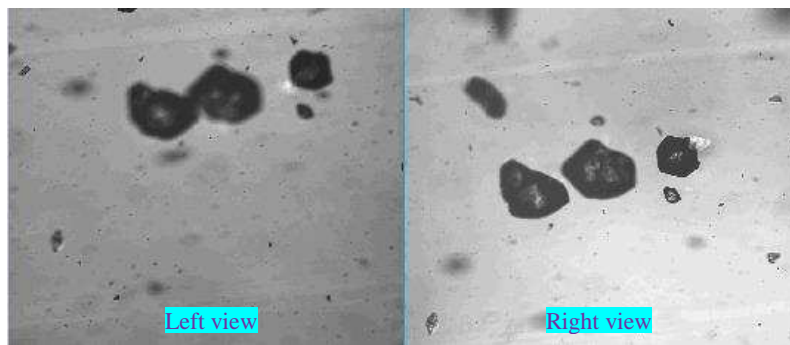


(a)



(b)

Figure 1. (a) Schematic of a microscopic image monitoring system for crystallization monitoring; (b) Experimental set-up of a non-invasive microscopic double-view imaging system



(a) Left view

(b) Right view

Figure 2. In-situ double-view images captured by a microscopic imaging system

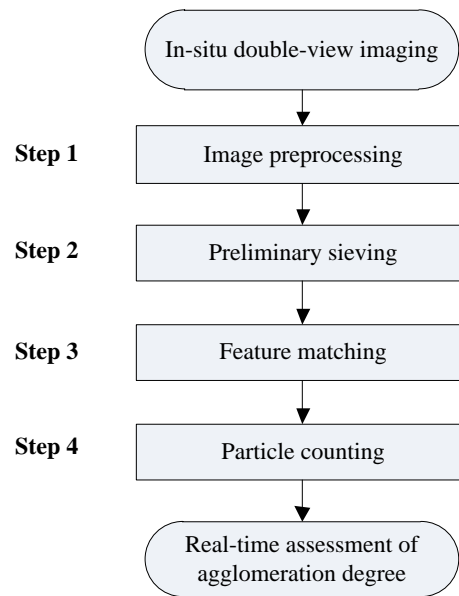


Figure 3. Flowchart of the proposed method for agglomeration detection

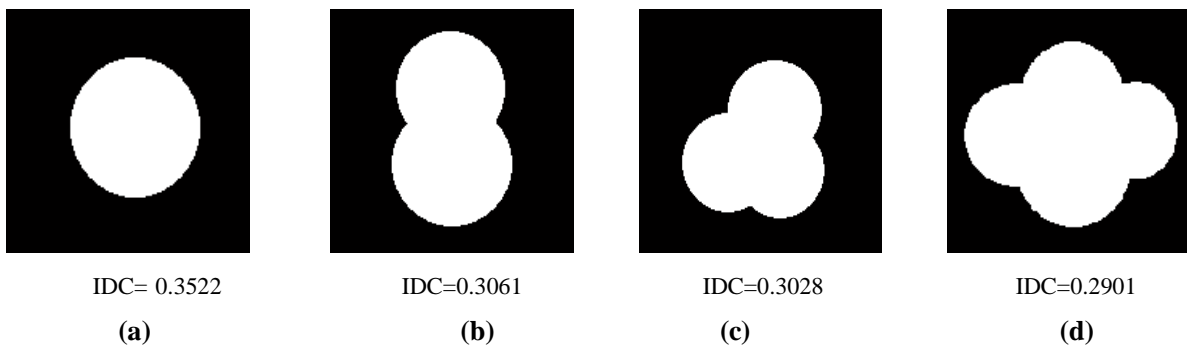


Figure 4. Illustration of IDC: (a) an unagglomerated particle; (b) agglomerate of two particles; (c) agglomerate of three particles; (d) agglomerate of four particles

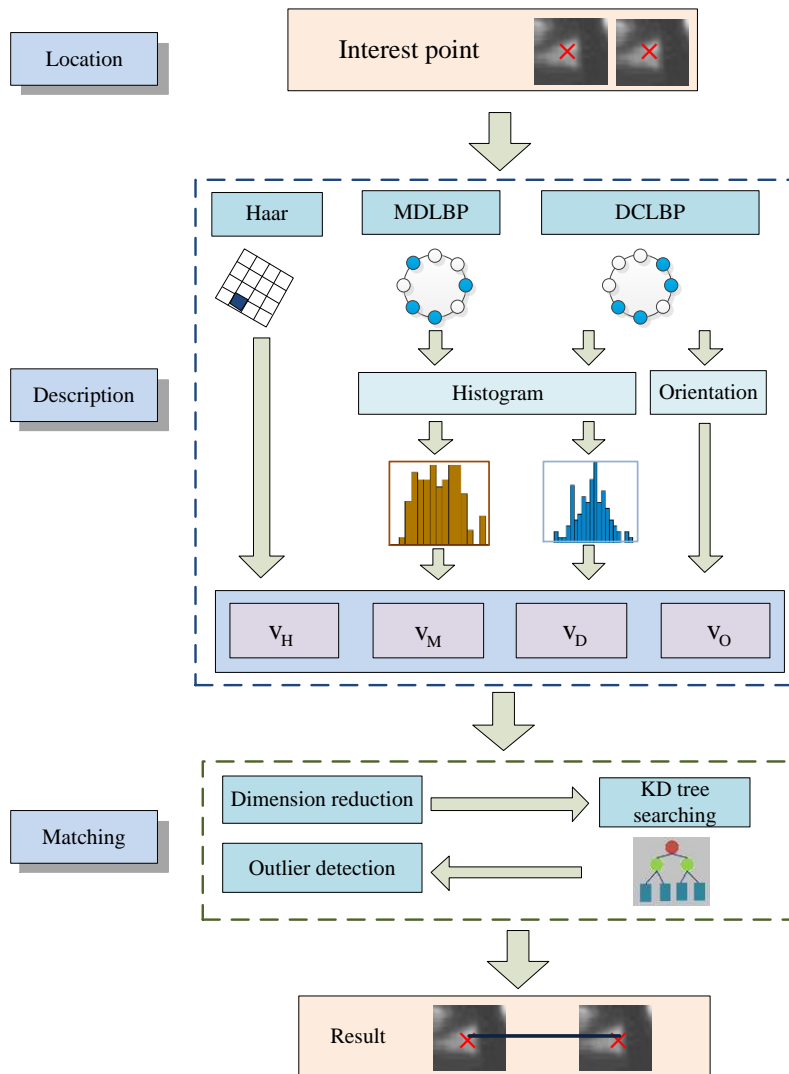


Figure 5. Flowchart of the proposed feature matching algorithm

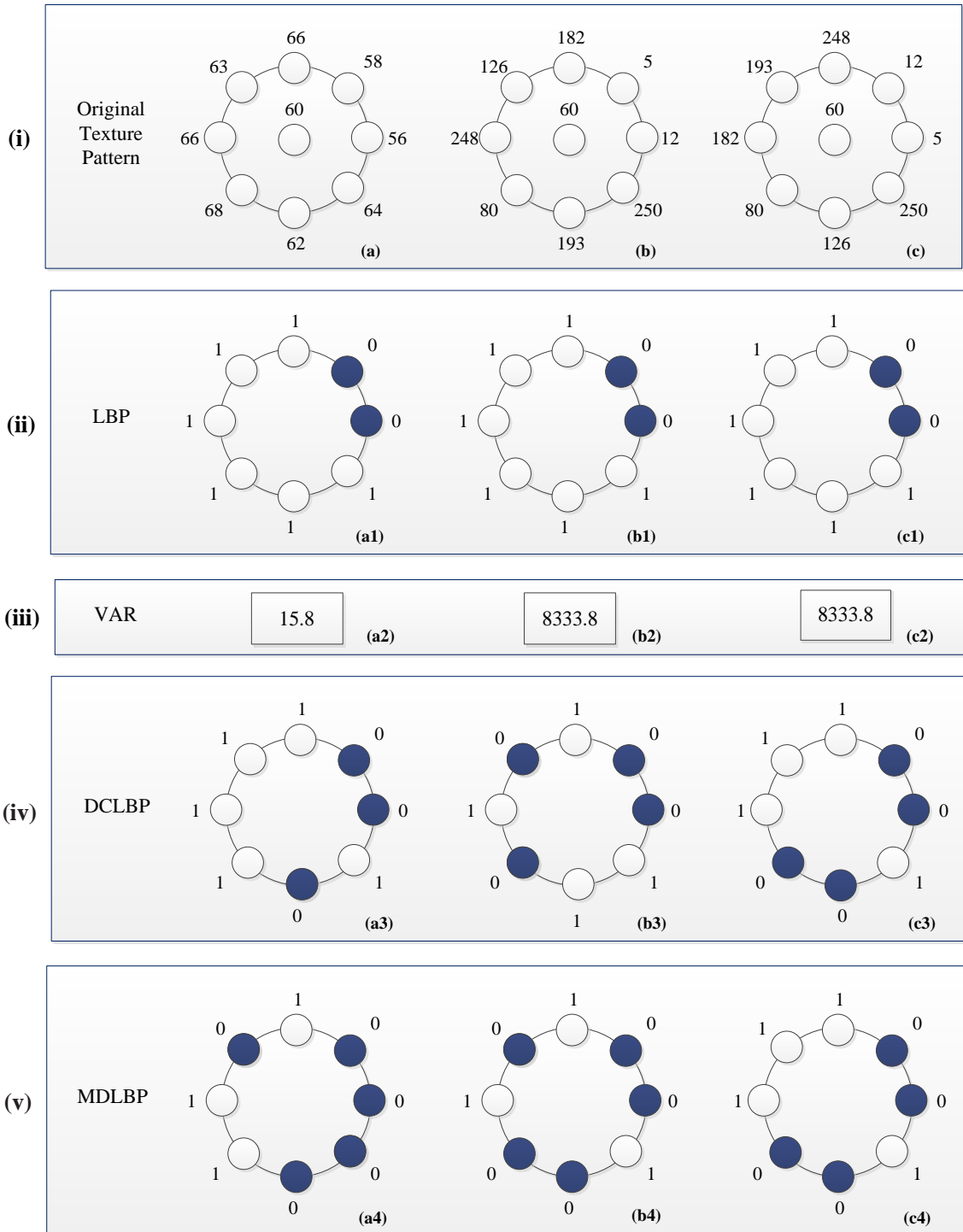


Figure 6. Comparison of texture recognition: (i) three different texture patterns (a, b, c); (ii) LBP (a1, b1, c1); (iii) VAR values (a2, b2, c2); (iv) DCLBP (a3, b3, c3); (v) MDLBP (a4, b4, c4)

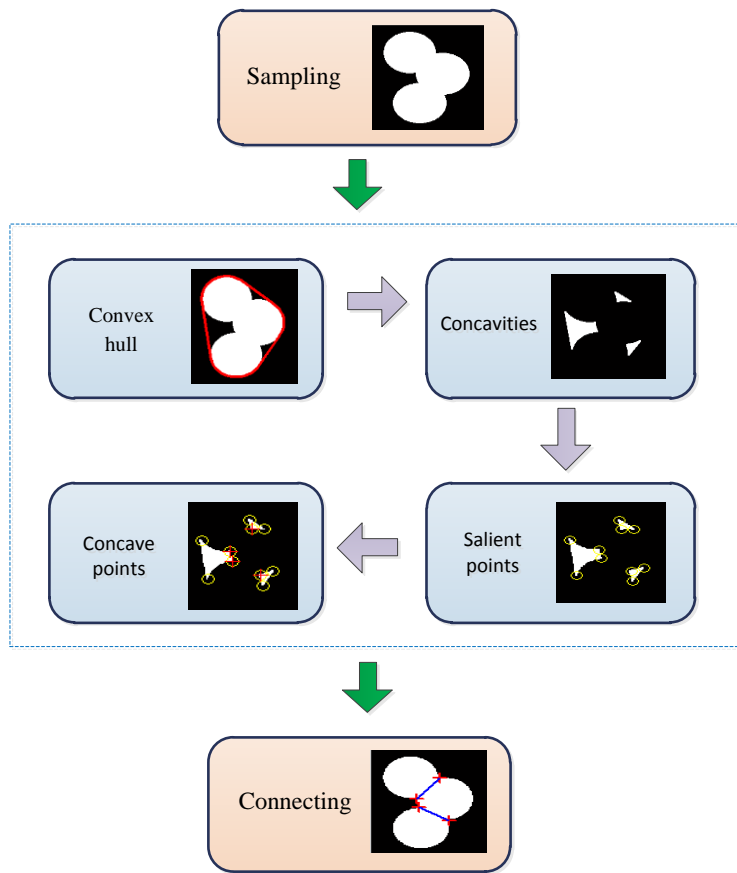
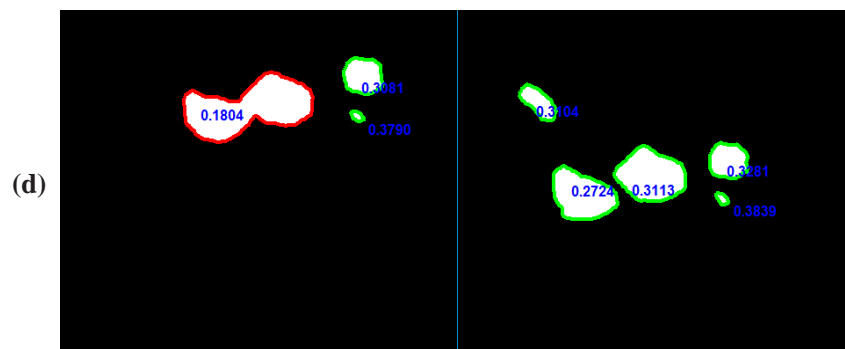
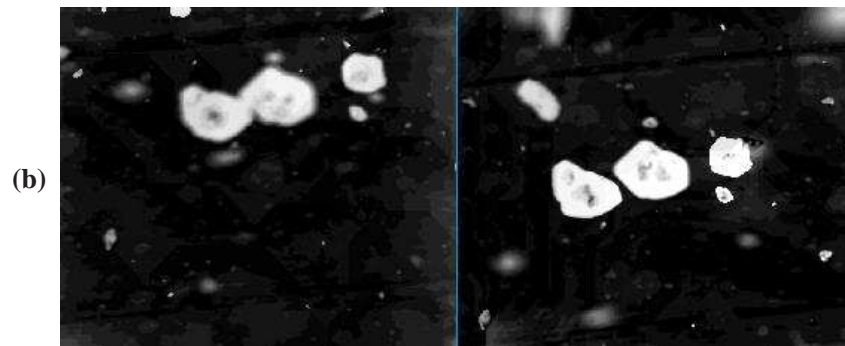
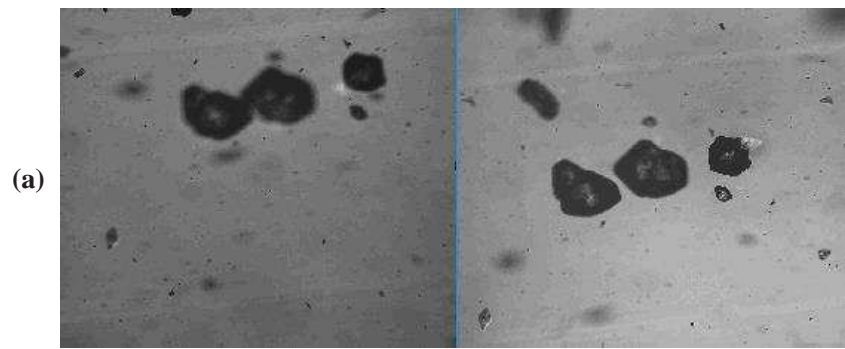


Figure 7. Schematic of the proposed counting algorithm for particle agglomerates



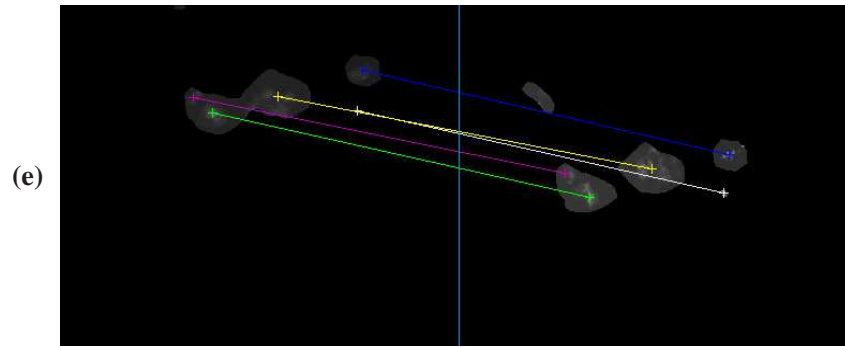


Figure 8. Double-view image processing for in-situ captured images: (a) preprocessed images; (b) result after removing the background; (c) segmented result; (d) preliminary sieving with IDC (a candidate agglomerate is labeled in red contour); (e) feature matching (the candidate agglomerate in the left view corresponds to two particles in the right view)

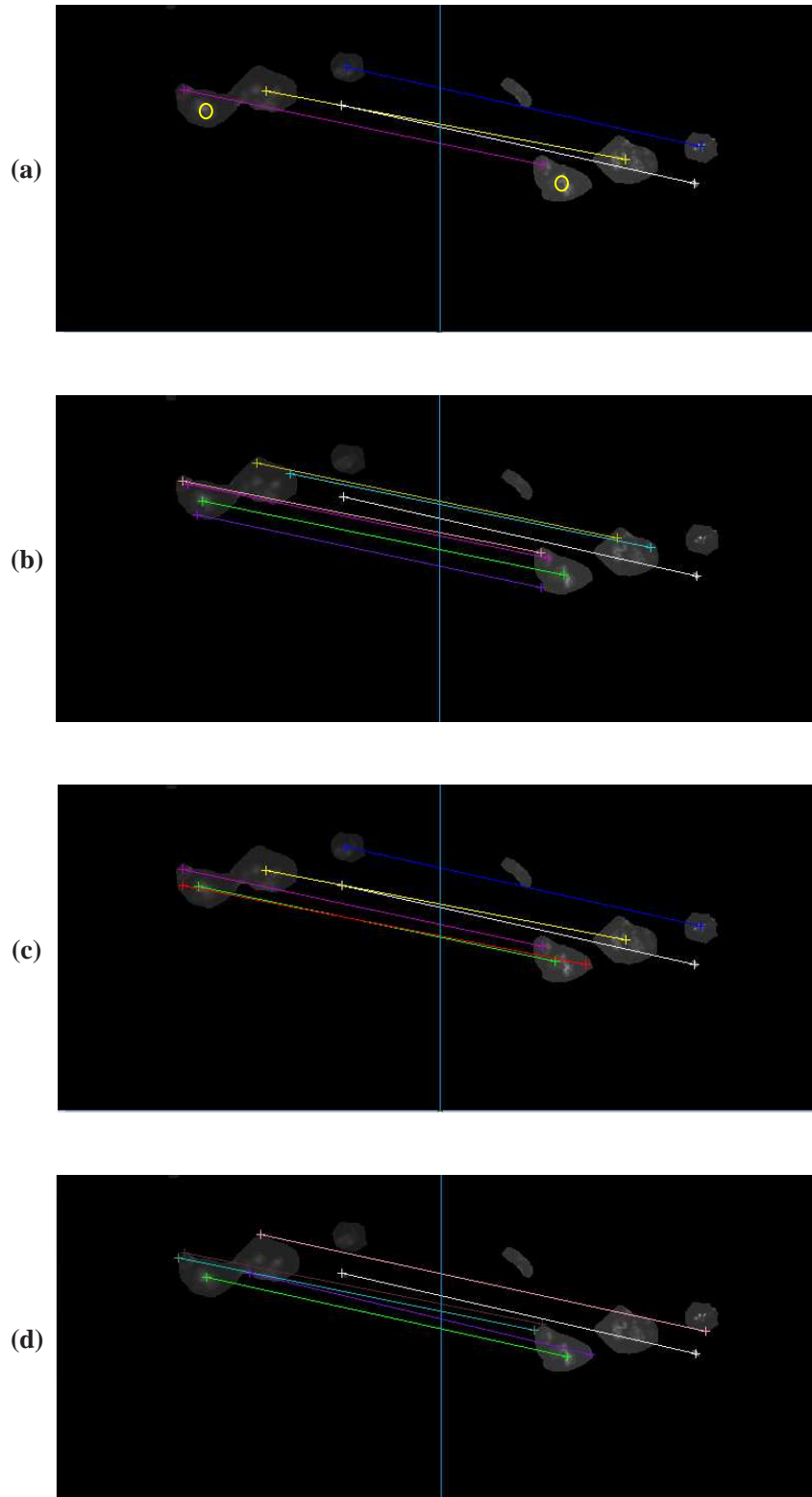


Figure 9. Comparison of matching results: (a) SIFT; (b) ASIFT; (c) SURF; (d) ORB

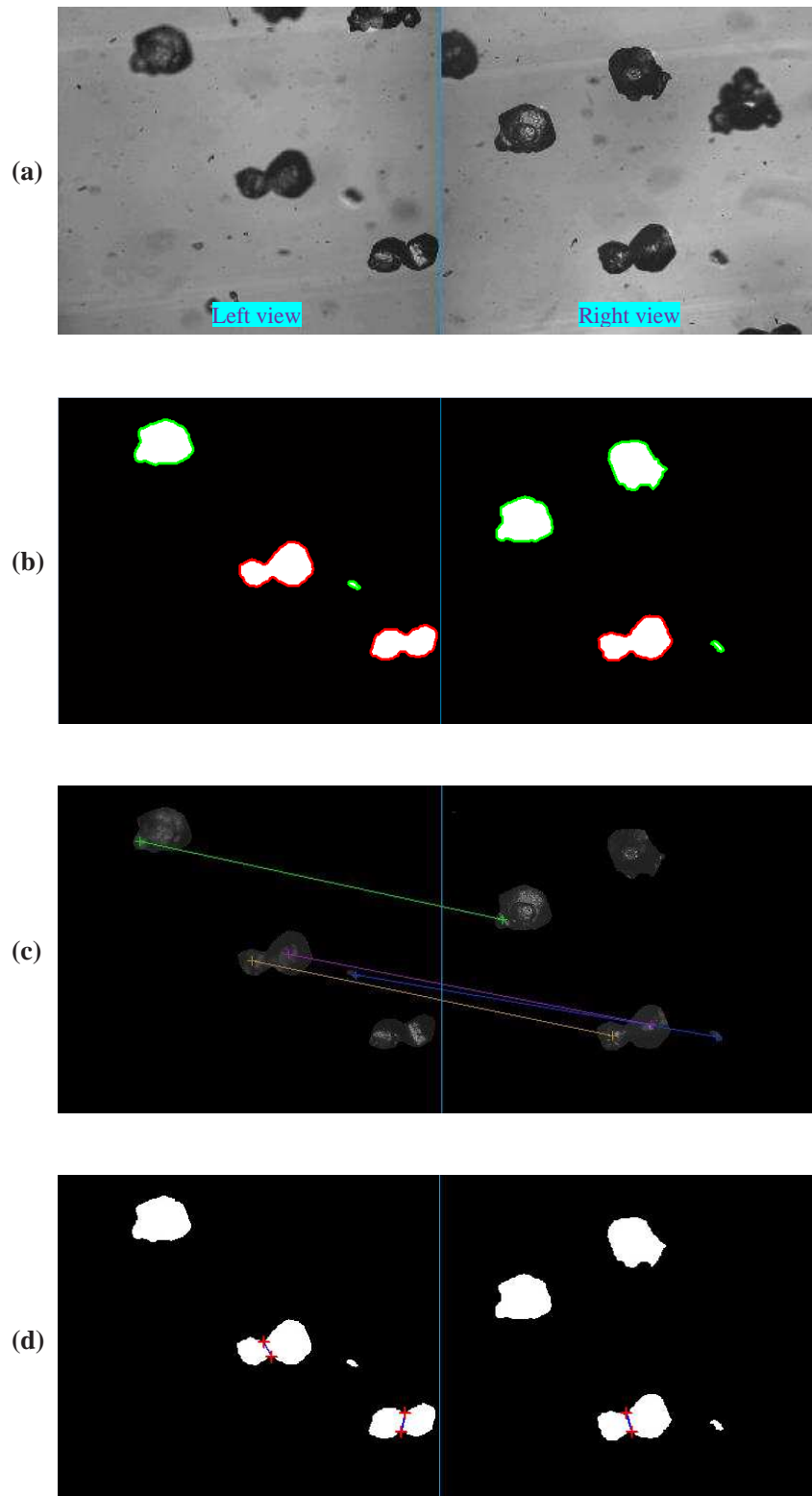


Figure 10. Agglomerate recognition and particle counting results: (a) in-situ captured double-view images; (b) preliminary sieving (candidate agglomerates are labeled with red contour); (c) feature matching; (d) counting primary particles in the agglomerates (the connecting lines indicating four primary particles in the two agglomerates in the left view)

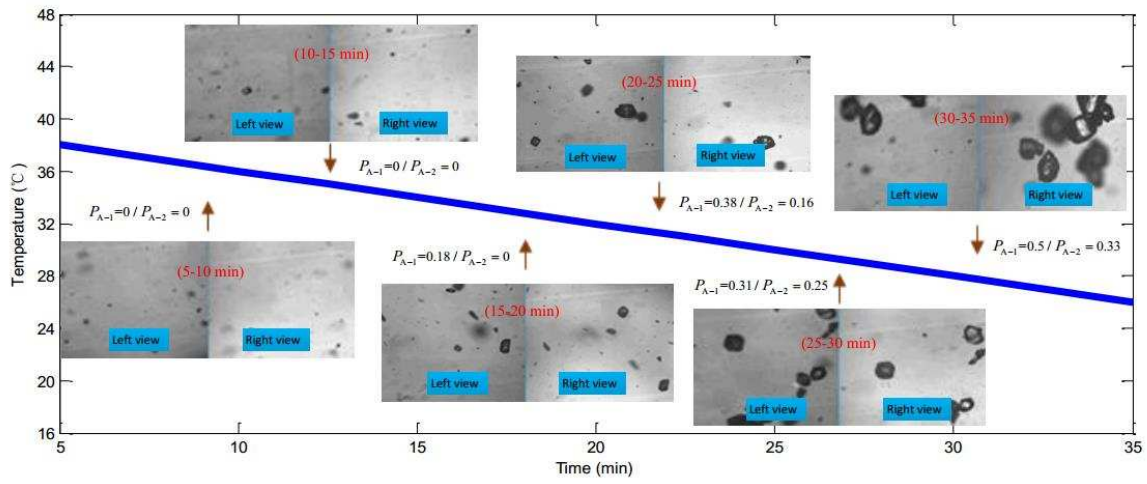


Figure 11. Microscopic double-view images captured during the KDP crystallization process